Improved oxygen evolution reaction performance in $Co_{0.4}Mn_{0.6}O_2$ nanosheets through Triple-doping (Cu, P, N) strategy and its application to Zn-air battery

Ying Li [a], Shamraiz Hussain Talib [b], Dongqing Liu [c], Kai Zong [a,d], Ali Saad [a,d], Zhaoqi Song [a], Jie Zhao [a], Wei Liu [a], Fude Liu [a], Qianqian Ji [e], Panagiotis Tsiakaras [f,*], Xingke Cai [a,*]

[a] *Institute for Advanced Study, Shenzhen University, Shenzhen, China*
[b] *Department of Chemistry and Key Laboratory of Organic Optoelectronics & Molecular Engineering of Ministry of Education, Tsinghua University, Beijing 100084, China*
[c] *College of Mechatronics and Control Engineering, Shenzhen University, Shenzhen 518060, China*
[d] *College of Physics and Optoelectronic Engineering, Shenzhen University, 518060, China*
[e] *National Synchrotron Radiation Laboratory, University of Science and Technology of China, China*
[f] *Laboratory of Alternative Energy Conversion Systems, Department of Mechanical Engineering, School of Engineering, University of Thessaly, 1 Sekeri Str., Pedion Areos 38834, Greece*

ARTICLE INFO

ABSTRACT

In this work, we successfully synthesized bimetallic transition oxides into two-dimensional nanosheets, which expose all the catalytic sites on the surface. Then, Cu, N, and P elements were rationally doped inside the as prepared $Co_{0.4}Mn_{0.6}O_2$ nanosheets to activate the Co/Mn catalytic sites. It is found that the resulting N/P-$Cu_{0.1}Co_{0.3}Mn_{0.6}O_2$/CNTs composites show an overpotential η_{10} of 290 mV for OER, much lower than the value measured using the original $Co_{0.4}Mn_{0.6}O_2$/CNTs (463 mV). Meanwhile, N/P-$Cu_{0.1}Co_{0.3}Mn_{0.6}O_2$/CNTs also show decent performance with a half potential ($E_{1/2}$) of 0.82 V vs RHE for ORR, i.e., a 702 mV voltage difference for OER and ORR, much lower than other transition metal oxide catalysts. By using N/P-$Cu_{0.1}Co_{0.3}Mn_{0.6}O_2$/CNTs as a cathodic catalyst for ZAB, we measured superior performance, with a peak power density of 108.1 mW cm^{-2} and stable operation for over 200 h at 10 mA cm^{-2}, better than IrO_2-Pt/C-based ZAB.

1. Introduction

Nowadays, humanity is facing serious energy crisis and environmental pollution mainly driven by the irrational use of fossil fuels. The use of renewable energy sources, such as solar, wind, hydropower and biomass, can help to overcome these challenges. The use of advanced energy storage systems is critical to store renewable energy for sustainable usage [1–3].

Among the energy storage systems, zinc-air batteries (ZAB) show comprehensive superiorities in various aspects, including high energy density, low production cost, inherent safety, and scalability [4–6]. However, the already commercialized ZAB are primary batteries, which cannot be recharged due to the easy growth of Zn dendrites in the anode and the sluggish oxygen evolution reaction (OER) and oxygen reduction reaction (ORR) kinetics in the cathode [7]. These drawbacks greatly limit their application in renewable energy storage stations and electric

vehicles, which require the repetitive storage and usage of the electric power conversed from the renewable energy sources.

In recent years, many efforts have been contributed to the development of secondary ZAB to expand their application in the field of rechargeable batteries. To accelerate the reaction kinetics in the cathode, catalysts for OER and ORR in an alkaline medium have to be used. The commercially available noble metal catalysts, such as Pt/C and IrO_2, exhibit decent performance at low current density, but they are not stable at high current density for long-term operation. Moreover, these high-cost catalysts only promote either ORR or OER. A mixture of them is needed to be used as catalysts in ZAB for accelerating both ORR and OER, but, as a result, only half of the catalysts of the total used amount work during the charge/discharge process [8,9]. To overcome these challenges, plenty of novel catalysts have been developed [10–12]. Among them, bimetallic transition metal oxides have emerged as the most promising alternatives to noble metal catalysts in terms of stability,

---

* Corresponding authors.
E-mail addresses: tsiak@uth.gr (P. Tsiakaras), cai.xingke@szu.edu.cn (X. Cai).

cost, and bifunctionality. However, their performance towards OER and ORR are not outstanding among the reported catalysts [13–16]. Many efforts have been contributed to enhance the performance of these bifunctional catalysts by increasing their surface area, i.e., the number of the catalytic sites, and mixing them with conductive carbon materials [17–19]. However, the intrinsic activity of their catalytic sites is still moderate. Strategies to improve the intrinsic activity of these bimetallic oxides are mainly focused on the ratio control of the two metallic elements, but the promotion effect is limited [20–22].

The doping of heteroatoms has been reported to show prominent regulation of the intrinsic activity of catalysts [23–25]. However, this strategy has rarely been used to tune the performance of bimetallic oxides. Nonmetallic dopants, such as N and P elements, are mainly doped into the conductive carbon materials, rather than the metallic oxides [26–28]. For instance, Dai et al. demonstrated that, during the preparation of nitrogen-doped Co_3O_4/rGO composites, the N atoms are not doped into the Co_3O_4 nanoparticles, but into the reduced graphene oxide (rGO) [29]. Only the Co atoms on the surface of the Co_3O_4 particles at the rGO/Co_3O_4 interface were influenced by the dopants, where a Co-N-C bond structure was formed. In this case, the promotion of the intrinsic activity of the Co catalytic sites by the nonmetallic dopants is limited. On the other hand, doping metallic elements inside bimetallic oxide nanoparticles contributes to multiple influences on their performance by forming metallic vacancies, inducing lattice stress, leading to a crystal structure change, etc [30–32]. Nevertheless, effectively controlling the structure and promotion effect in bimetallic oxides through metal elements doping is still challenging. Therefore, for efficiently improving the performance of bimetallic transition metal oxides by heteroatoms doping, the effective doping on all the catalytic sites with good controllability on the structure and performance is quite important.

Bimetallic 3d transition metal (Fe, Co, Mn, Ni) oxides can simultaneously catalyze both reactions of oxygen evolution and oxygen reduction (OER and ORR) in an alkaline medium, demonstrating their potential as catalysts for Zn-air battery (ZAB) applications. However, despite their advantages in costs, scalability, and bifunctionality, their intrinsic activity is limited.

In this work, we provide a strategy to efficiently dope heteroatoms inside bimetallic oxides by fabricating them into a 2D structure and then doping them by a mixing and post-doping strategy. The coordination environment of the metallic catalytic sites on these 2D materials can be very easily modified. Firstly, we successfully doped metallic (Cu) heteroatoms inside the cobalt manganese oxides to form $Cu_{0.1}Co_{0.3}Mn_{0.6}O_2$ nanosheets by mixing doping Cu inside the layered precursors. Then, a post-doping strategy was used to dope N and P elements inside the nanosheets to further improve their OER/ORR performance. Due to the efficient regulation of the Cu, P, and N atoms on the number and the intrinsic activity of active Co catalytic sites, the as-formed N/P-$Cu_{0.1}Co_{0.3}Mn_{0.6}O_2$/CNTs show 160 mV lower overpotential at 10 mA·cm^{-2} than $Co_{0.4}Mn_{0.6}O_2$/CNTs for OER. The Cu, P, and N triple element-doped nanosheets also show decent ORR performance with an $E_{1/2}$ of 0.82 V vs RHE and better ZAB performance than the IrO$_2$-Pt/C-based catalyst in terms of stability, peak power density, and voltage gap.

2. Experimental section

2.1. Synthesis of $Cu_{0.1}Co_{0.3}Mn_{0.6}O_2$ and $Co_{0.4}Mn_{0.6}O_2$ nanosheets

The $Cu_{0.1}Co_{0.3}Mn_{0.6}O_2$ nanosheets were prepared through the following procedures, including the synthesis of layered $Na_{0.6}Cu_{0.1}$-$Co_{0.3}Mn_{0.6}O_2$, its protonation, and exfoliation (Fig. S1). Firstly, the starting material of layered $Na_{0.6}Cu_{0.1}Co_{0.3}Mn_{0.6}O_2$ was synthesized via a solution route, as previously reported [33]. The salts of $NaNO_3$, Cu $(CH_3COO)_2·H_2O$, $Co(CH_3COO)_2·0.4 H_2O$, and $Mn(CH_3COO)_2·0.4 H_2O$ in a stoichiometric ratio of 0.6:0.1:0.3:0.6 were dissolved in deionized water. To realize a uniform mixture of the metallic ions, the solution was

dried on a hot plate at 150 °C. Then, the precipitates were calcined at 800 °C for 20 h in a furnace in the air to remove the organic components. After cooling down, the layered precursor $Na_{0.6}Cu_{0.1}Co_{0.3}Mn_{0.6}O_2$ was obtained. The second step is the protonation process. The obtained $Na_{0.6}Cu_{0.1}Co_{0.3}Mn_{0.6}O_2$ powder was grounded, dispersed, and stirred evenly in a diluted hydrogen chloride (HCl: 0.5 mol dm^{-3}) solution. The HCl solution was replaced every 24 h, and the procedure was repeated four times to realize the acid exchange of Na$^+$ to H$^+$. Then, the protonic product H-$Cu_{0.1}Co_{0.3}Mn_{0.6}O_2$ was rinsed with deionized water several times and dried in air. The protonic product (H-$Cu_{0.1}Co_{0.3}Mn_{0.6}O_2$, 0.62 g) was added into a 168 mL tetrabutylammonium hydroxide solution (TBAOH, ~0.5 wt%) and stirred at 180 rpm for two weeks. The upper solution after a 3000-rpm centrifugation was collected, which was the $Cu_{0.1}Co_{0.3}Mn_{0.6}O_2$ nanosheets suspension. For the preparation of $Co_{0.4}Mn_{0.6}O_2$ nanosheets, the procedure is the same but without the addition of a Cu precursor.

2.2. Synthesis of N, P co-doped $Cu_{0.1}Co_{0.3}Mn_{0.6}O_2$ nanosheets/CNTs composite

An equivalent amount of a freeze-dried $Cu_{0.1}Co_{0.3}Mn_{0.6}O_2$ nanosheets powder (20 mg) and carbon nanotubes (CNTs, 20 mg) were dissolved in ethanol (30 mL) and ultrasonically treated for two hours to mix them homogenously. Another solution was prepared by slowly dropping the phosphoric acid (H_3PO_4) into ammonia under a molecular ratio of 1:4 until they reacted completely. Then, the two solutions were mixed by ultrasonication for 30 min and then placed in a hydrothermal reactor and heated at 150 °C for 3 h. The resulting product of $Co_{0.3}Mn_{0.6}$-$Cu_{0.1}O_{2-x}N_yP_z$/CNTs was collected by filtration and repeatedly rinsed with deionized water. The same procedure was applied to prepare $Co_{0.3}Mn_{0.6}Cu_{0.1}O_{2-x}N_y$/CNTs and $Co_{0.3}Mn_{0.6}Cu_{0.1}O_2$/CNTs for comparison.

2.3. Materials characterizations

The X-ray diffraction patterns were collected by an Ultima IV instrument with monochromatic Cu Kα radiation (0.15404 nm). The scanning electron microscopy (SEM, Hitachi SU8010, 15 kV, Japan) coupled with energy-dispersive X-ray spectroscopy (EDS) was applied to observe the morphology of the samples and obtain their chemical composition. The size and thickness of the exfoliated nanosheets were measured by the tapping mode of Atomic Force Microscopy (AFM, Bruker Dimension Icon, Germany). Transmission Electron Microscopy (TEM, FEI Tecnai G2 F20, USA) was used to determine the microstructure of the samples at a nanoscale resolution. The chemical state of each element in the samples was examined by X-ray photoelectron spectroscopy (XPS, PHI Versa Probe II, Japan) with mono-energetic Al Kα X-rays. The contents of Cu, Co, and Mn elements inside each sample were determined by inductively coupled plasma emission spectroscopy (ICP, MDTC-EQ-M29–01, USA). The ultraviolet-visible (UV-Vis) spectra were recorded on a spectrophotometer (TU-1901, China). The surface areas of the samples were recorded by the BET instrument (autosorb iQ, USA).

2.4. Electrochemical measurements

The electrochemical tests were carried out on a modulated speed rotator (MSR, PINE, USA) system connected with a Chenhua electrochemical station (CHI 760e, China) in a 1.0 M KOH electrolyte. A glassy carbon rotating disk electrode (RDE) loaded with catalysts was used as a working electrode. Ag/AgCl and Pt foil work as a reference and counter electrode. For the preparation of the catalysts on the working electrode, the ink, composed of 5 mg catalyst, 30 μl Nafion, and 970 μl solvent ($V_{alcohol}$: V_{water} = 1: 1), was firstly sonicated for 30 min; then, 10 μl of the ink was dropped evenly onto the surface of the glass carbon and dried at room temperature. Prior to the OER and ORR tests, the electrolyte was purged with oxygen for 30 mins to reach an oxygen saturation state.
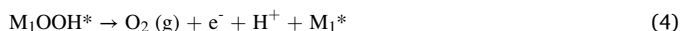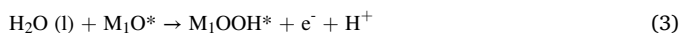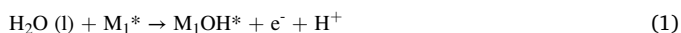
Before the electrochemical tests, cyclic voltammetry (CV) at a scan rate of 100 mV s^{-1} was performed to activate the catalyst until the curve became stable. Then, the linear sweep voltammetry (LSV) was carried out at a scan rate of 5 mV s^{-1} in the potential range of 1.2–1.8 V vs. RHE and 1.25–0.1 V vs. RHE for OER and ORR, respectively. The rotating speed of the working electrode was set to 1600 rpm. The electrochemical impedance spectroscopy (EIS) was collected at a potential of 1.52 V vs. RHE with an amplitude of 5 mV from 0.001 to 1000 kHz. The double-layer capacitance values (C_{dl}) were determined by CV curves from 0.1 to 0.3 V vs. RHE at various scan rates (20–140 mV s^{-1}).

For the ZAB performance, a full cell was assembled by using a zinc plate as the anode and a catalyst-loaded tri-layer composite substrate (carbon paper, PTFE waterproof layer, and Ni foam) as the cathode. The electrolyte used was 6 M KOH and 0.2 M zinc acetate. 4 mg of the catalysts was dissolved in a solution of ethanol and water ($V_{ethanol}$: V_{water} = 3:1) and sonicated for 30 min. Then, the ink was dropped uniformly on the composite substrate and dried under an infrared lamp. For the zinc anode, it was polished with sandpaper to remove the surface oxide and rinsed with ethanol prior to use. For comparison, IrO_2-Pt/C under a weight ratio of 1:1 with the same total weight with $Co_{0.3}Mn_{0.6}$-$Cu_{0.1}O_{2-x}N_yP_z$/CNTs was also coated on the composite substrate to fabricate the ZAB, which was named as IrO_2-Pt/C-based ZAB.

2.5. Computational details

All of the calculations were performed by means of the spin-polarized density functional theory (DFT) methods using the Vienna ab-initio simulation package (VASP) [34,35]. The Perdew-Burke-Ernzerhof (PBE) combined with generalized gradient approximation functional (GGA) was employed to describe the exchange-correlation energy [36,37]. Blöchl's all-electron-like projector augmented wave (PAW) formalism was used to describe the interactions between all the electrons and the frozen core [38,39]. The plane-wave basis set was used to expand the electron wave functions. In this work, the kinetic energy (KE) cutoff was chosen as 450 eV. The Brillouin zone integration was sampled by a specially selected k-points using the Gamma-centered Monkhorst–Pack grid, which was set to $3 \times 3 \times 1$ [40]. The electron occupancies were determined according to the Fermi scheme with an energy smearing of 0.1 eV. The energy convergence was set to 1.0×10^{-6} eV, and the residual force on each atom was smaller than 0.01 eV/Å for the structural relaxations. To avoid the periodic interactions between two periodically repeated units, a vacuum space exceeding 15 Å was employed along the z-direction. By using the standard hydrogen electrode (SHE), the Gibbs free energy change (ΔG) of every elemental step was calculated.

The following are the four electron reaction steps for the OER process: [41].

$$H_2O \ (l) + M_1^* \rightarrow M_1OH^* + e^- + H^+ \quad (1)$$

$$M_1OH^* \rightarrow M_1O^* + e^- + H^+ \quad (2)$$

$$H_2O \ (l) + M_1O^* \rightarrow M_1OOH^* + e^- + H^+ \quad (3)$$

$$M_1OOH^* \rightarrow O_2 \ (g) + e^- + H^+ + M_1^* \quad (4)$$

The Gibbs free energy difference for all the above elementary steps ($ΔG_{OOH^*}$, $ΔG_{O^*}$, $ΔG_{OH^*}$), containing an electron transfer, can be calculated by using the following equations:

$$ΔG = ΔE + ΔZPE - TΔS + ΔG_U + ΔG_{pH} \quad (5)$$

Where ΔE, ΔZPE, and ΔS correspond to the energy difference among the free-standing and the adsorption states of the reaction intermediates and the changes in the zero-point energies and the entropy, respectively. The adsorption energies of ΔE are directly obtained from the DFT calculations. $ΔG_U$ = -eU, where e and U are the number of electrons transferred and it signifies the potential based on the SHE. $ΔG_{pH}$ signifies

the Gibbs free energy correction of the pH, which can be calculated by: $ΔG_{pH}$ = -k_BTln10*pH, where k_B denotes the Boltzmann constant (1.380649 $\times 10^{-23}$ JK^{-1}) and T the temperature of 298.15 k. The vibrational frequencies and entropies of the molecules in the gas phase were taken from the NIST database.

The Gibbs free energy changes of the four elementary steps for the OER process can be defined as: $ΔG_a = ΔG_{OH^*}$, $ΔG_b = ΔG_{O^*} - ΔG_{OH^*}$, $ΔG_c = ΔG_{OOH^*} - ΔG_{O^*}$, $ΔG_d = 4.92 - ΔG_{OOH^*}$.

If the ΔG values of all the four elementary steps are different, the overpotential (η) used to further justify the catalytic activity of OER can be calculated by using the following equations:

$$η^{OER} = max \ \{ΔG_a, ΔG_b, ΔG_c, ΔG_d\}/e - 1·23 \quad (6)$$

3. Results and discussion

3.1. Preparation and characterization of $Cu_{0.1}Co_{0.3}Mn_{0.6}O_2$ nanosheets

As schematically illustrated in Fig. 1a, the $Cu_{0.1}Co_{0.3}Mn_{0.6}O_2$ nanosheets were fabricated through three synthetic steps: the synthesis of $Na_{0.6}Cu_{0.1}Co_{0.3}Mn_{0.6}O_2$, its protonation to H-$Cu_{0.1}Co_{0.3}Mn_{0.6}O_2$ by an HCl solution, and the exfoliation of the protonated layered structure into $Cu_{0.1}Co_{0.3}Mn_{0.6}O_2$ nanosheets. Firstly, we characterized the structural and compositional evolution during the $Cu_{0.1}Co_{0.3}Mn_{0.6}O_2$ nanosheets preparation process. From the X-ray diffraction (XRD) patterns (Fig. 1b), the $Na_{0.6}Cu_{0.1}Co_{0.3}Mn_{0.6}O_2$ precursor is indexed to a rhombohedral crystal structure, same as the reported $Na_{0.6}Co_{0.4}Mn_{0.6}O_2$ [33]. After the incorporation of the Cu atoms to replace the Co atoms, the position of the strongest layered peak corresponding to the (003) facet essentially shows no change, indicating that the substitution of Co with Cu atoms does not induce an interlayer interaction change but an in-plane bond structure change. After the protonation process, both H-$Co_{0.4}Mn_{0.6}O_2$ and H-$Cu_{0.1}Co_{0.3}Mn_{0.6}O_2$ samples remain layered structured but with a much larger interlayer distance than their pristine alkaline metal-containing layered structure, as indicated by their shifted peaks towards smaller diffraction angle compared to $Co_{0.4}Mn_{0.6}O_2$ and $Cu_{0.1}Co_{0.3}Mn_{0.6}O_2$, respectively [42].

The scanning electron microscopy (SEM) images for the $Na_{0.6}Cu_{0.1}Co_{0.3}Mn_{0.6}O_2$ and H-$Cu_{0.1}Co_{0.3}Mn_{0.6}O_2$ further confirm that the layered structure has been well preserved after the protonation (Fig. 1c-d), but the layer spacing has been expanded. These results indicate that the Cu doping does not really influence a proton exchange process between the metals in the layered $Na_{0.6}Co_{0.4}Mn_{0.6}O_2$. The corresponding element distribution, analyzed by energy-dispersive X-ray spectroscopy (EDS) (Figs. 1e and S2), clearly indicates the Na element disappearance, confirming a successful protonation process.

After a mechanical shaking process to fully exfoliate the protonated sample in a TBAOH solution, a $Cu_{0.1}Co_{0.3}Mn_{0.6}O_2$ suspension was obtained. The Tyndall effect with a clear "light path" can be observed in the $Cu_{0.1}Co_{0.3}Mn_{0.6}O_2$ nanosheets aqueous suspension along the direction of a light beam, indicating a good exfoliation and uniform dispersion of the nanosheets (Fig. S3). In Fig. S4a, the UV–visible absorption spectrum of the $Cu_{0.1}Co_{0.3}Mn_{0.6}O_2$ nanosheet suspension show an absorption peak at ~360 nm, similar to the MnO_2 nanosheets, which is attributed to the transition from the occupied valence band (O 2p orbital) to the unoccupied conduction band (metal 3d orbit) [33,43]. Compared with the $Co_{0.4}Mn_{0.6}O_2$ nanosheets, the absorption edge of $Cu_{0.1}Co_{0.3}Mn_{0.6}O_2$ nanosheets is towards smaller diffraction angle due to the Co atoms replacement with the Cu atoms, which can increase the electrons in the metal-based conduction band and shift the Fermi level to more negative energy [44]. This observation suggests the successful doping of Cu atoms and their homogenous distribution in the host lattice. The inductively coupled plasma (ICP) measurement found that the element ratio of Cu: Co: Mn in the $Cu_{0.1}Co_{0.3}Mn_{0.6}O_2$ nanosheets is 10.6:
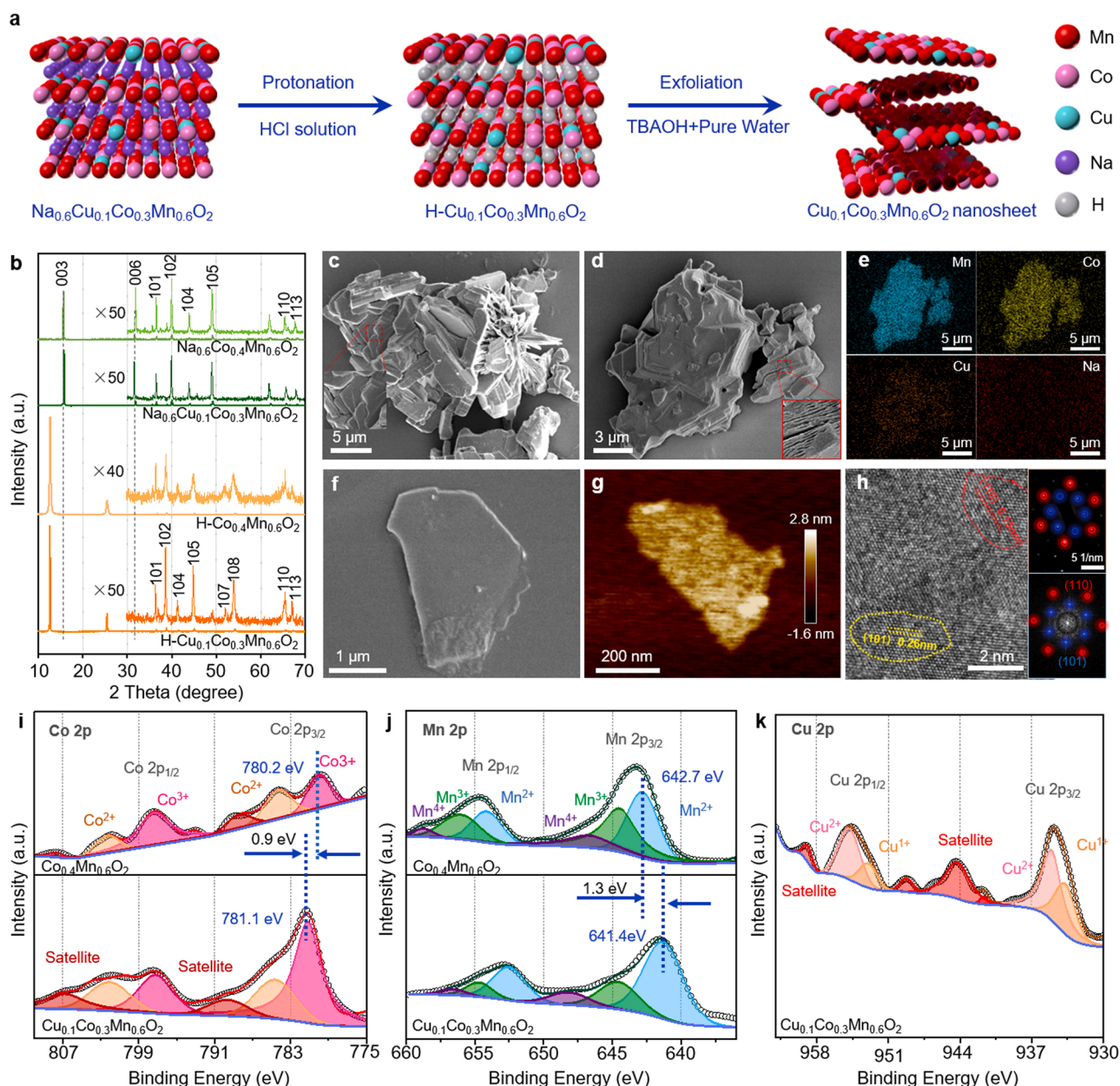
Fig. 1. (a) Schematic illustration of the preparation procedure of $Cu_{0.1}Co_{0.3}Mn_{0.6}O_2$ nanosheets; (b) XRD patterns of $Na_{0.6}Co_{0.4}Mn_{0.6}O_2$, $Na_{0.6}Cu_{0.1}Co_{0.3}Mn_{0.6}O_2$, H-$Co_{0.4}Mn_{0.6}O_2$, and H-$Cu_{0.1}Co_{0.3}Mn_{0.6}O_2$; (c) SEM of $Na_{0.6}Cu_{0.1}Co_{0.3}Mn_{0.6}O_2$; (d, e) SEM of H-$Cu_{0.1}Co_{0.3}Mn_{0.6}O_2$ and its EDS images; (f, g) SEM and AFM image of $Cu_{0.1}Co_{0.3}Mn_{0.6}O_2$ nanosheets; (h) HR-TEM image of the $Cu_{0.1}Co_{0.3}Mn_{0.6}O_2$ nanosheets (top inset: SAED pattern; bottom inset: FFT pattern of the full image); (i-k) The XPS spectra of $Co_{0.4}Mn_{0.6}O_2$ and $Cu_{0.1}Co_{0.3}Mn_{0.6}O_2$ for i) Co 2p, (j) Mn 2p and (k) Cu 2p.

30.5: 58.9 (Fig. S4b), close to the nominal value of 10: 30: 60. This result indicates that the exfoliation process didn't change the original composition of the host layers.

Then, the structure of the as-obtained $Cu_{0.1}Co_{0.3}Mn_{0.6}O_2$ nanosheets was characterized. The SEM image indicates that the ultrathin $Cu_{0.1}Co_{0.3}Mn_{0.6}O_2$ was obtained after the exfoliation process (Fig. 1f). The atomic force microscopy (AFM) observation shows the flat surface of the nanosheets with a lateral size of 0.5–0.8 μm and an average thickness of ~1 nm (Fig. 1g). The high-resolution transmission electron microscopy (HRTEM) image in Fig. 1h shows a clear lattice structure, suggesting the well-crystallized in-plane structure of the $Cu_{0.1}Co_{0.3}Mn_{0.6}O_2$ nanosheets. The selected area electron diffraction (SAED) and Fast Fourier Transform (FFT) patterns of the whole image are consistent with each other and correlate well with the peaks of the XRD pattern, indicating that the in-plane structure of the

$Cu_{0.1}Co_{0.3}Mn_{0.6}O_2$ layer has been well preserved during the whole exfoliation process.

XAFS and XPS were further applied to explore the chemical state change of each element after the Cu doping inside the $Co_{0.4}Mn_{0.6}O_2$ nanosheets. The $Co_{0.4}Mn_{0.6}O_2$ nanosheets sample contains mixed cations of Co (Co^{2+}, Co^{3+}) and Mn (Mn^{2+}, Mn^{3+}, Mn^{4+}), as shown in Figs. 1i-j and S5. According to the XAFS spectra of Co L-edge and Mn L-edge, the mixed charge states for Co are between 2 + and 3 + , and for Mn are between 2 + and 4 + . Then, we deconvoluted the spectra for them to analyze the ratio of each charge state. Three peaks at 780.2, 784.1, and 788.7 eV have been revealed in Co $2p_{3/2}$, which are attributed to Co^{3+}, Co^{2+}, and its shake-up satellite peak, respectively. The deconvolution of Mn $2p_{3/2}$ illustrated three peaks (Mn^{2+} = 642.7 eV, Mn^{3+}=644.5 eV, Mn^{4+}=646.9 eV), as well. With the incorporation of the low charge state Cu (Cu^{1+}, Cu^{2+}), the oxidation states of Co and Mn

all changed (Figs. 1i-k and Fig. S6). The deconvolution of Co 2p$_{3/2}$ peak reveals three peaks at 781.1, 784.7 and 789.8 eV, which are attributed to the Co^{3+}, Co^{2+} and its shake-up satellite peak. Mn 2p spectrum is then deconvoluted into three peaks, corresponding to Mn^{2+} (Mn 2p$_{3/2}$ at 641.4 eV), to Mn^{3+} (Mn 2p$_{3/2}$ at 644.4 eV) and to Mn^{4+} (Mn 2p$_{3/2}$ at 648.1 eV). The Cu 2p$_{3/2}$ peak has three peaks at 933.9, 935.1 and 944.3 eV, which represented the Cu^{3+}, Cu^{2+} and its shake-up satellite peak. Compared with the Co$_{0.4}$Mn$_{0.6}$O$_2$ nanosheets, the Co 2p spectrum of the Cu$_{0.1}$Co$_{0.3}$Mn$_{0.6}$O$_2$ nanosheets shows a general shift towards higher binding energies, and the Mn 2p spectrum of the Cu$_{0.1}$Co$_{0.3}$Mn$_{0.6}$O$_2$ nanosheets shows a general shifting to lower binding energies. Specifically, the Co^{3+} shifts by 0.9 eV (from 780.2 eV for 2p3/ 2 orbital of Co$_{0.4}$Mn$_{0.6}$O$_2$ to 781.1 eV for those of Cu$_{0.1}$Co$_{0.3}$Mn$_{0.6}$O$_2$) towards higher binding energy, and Mn^{2+} shifts by more than 1.3 eV towards lower binding energy (from 642.7 eV to 641.4 eV). This change could be correlated with the Fermi level energy regulation of Co and Mn after Cu doping, which was also indicated previously by UV–vis adsorption spectra (Fig. S3a). The absorption peak for Co ions shifted towards longer wavelengths, and the Mn ions shifted towards shorter wavelengths after Cu doping, indicating the energy band for Mn atoms moved away from the Fermi level, and the energy band for Co atoms moved close to the Fermi level. Consequently, these positively charged Co atoms show an increased adsorption towards the negatively charged OH$^-$ ions and the Mn atoms show an increased desorption towards OH$^-$

ions. The adsorption of the -OH species on the Co catalytic sites is the first step for OER, which means the better adsorption towards -OH species can facilitate the OER kinetics. On the other hand, the better desorption of the produced -OH species from the Mn catalytic sites can accelerate the ORR kinetics. Previous studies indicate that the Cu dopant can improve the OER performance of the Co$_3$O$_4$ film [20,45] and ORR performance of the MnO$_2$ film [46] in an alkaline medium. Therefore, we can predict that the doping of Cu inside the Co$_{0.4}$Mn$_{0.6}$O$_2$ nanosheets will enhance its OER and ORR performance.

3.2. Preparation and characterization of N/P-Cu$_{0.1}$Co$_{0.3}$Mn$_{0.6}$O$_2$/CNTs composite

A post-doping strategy was used to dope the nonmetallic N and P elements inside the Co$_{0.3}$Mn$_{0.6}$Cu$_{0.1}$O$_2$ nanosheets to further regulate the electronic structures of the catalytic sites. Since these oxide nanosheets are insulating, conductive carbon nanotubes (CNTs) are mixed with them to facilitate the charge transfer at the interface of the electrode/electrolyte. In previous reports, the N and P atoms tend to be doped inside carbon materials due to the oxygen functional groups on them [19, 21, 26–28, 47]. Their doping into the crystalline metal oxides has been rarely reported, but in these cases, the dopants are totally transformed into other compounds [48,49]. In our case, we prepared a bimetallic oxide of ultrathin nanosheets with all the metallic atoms
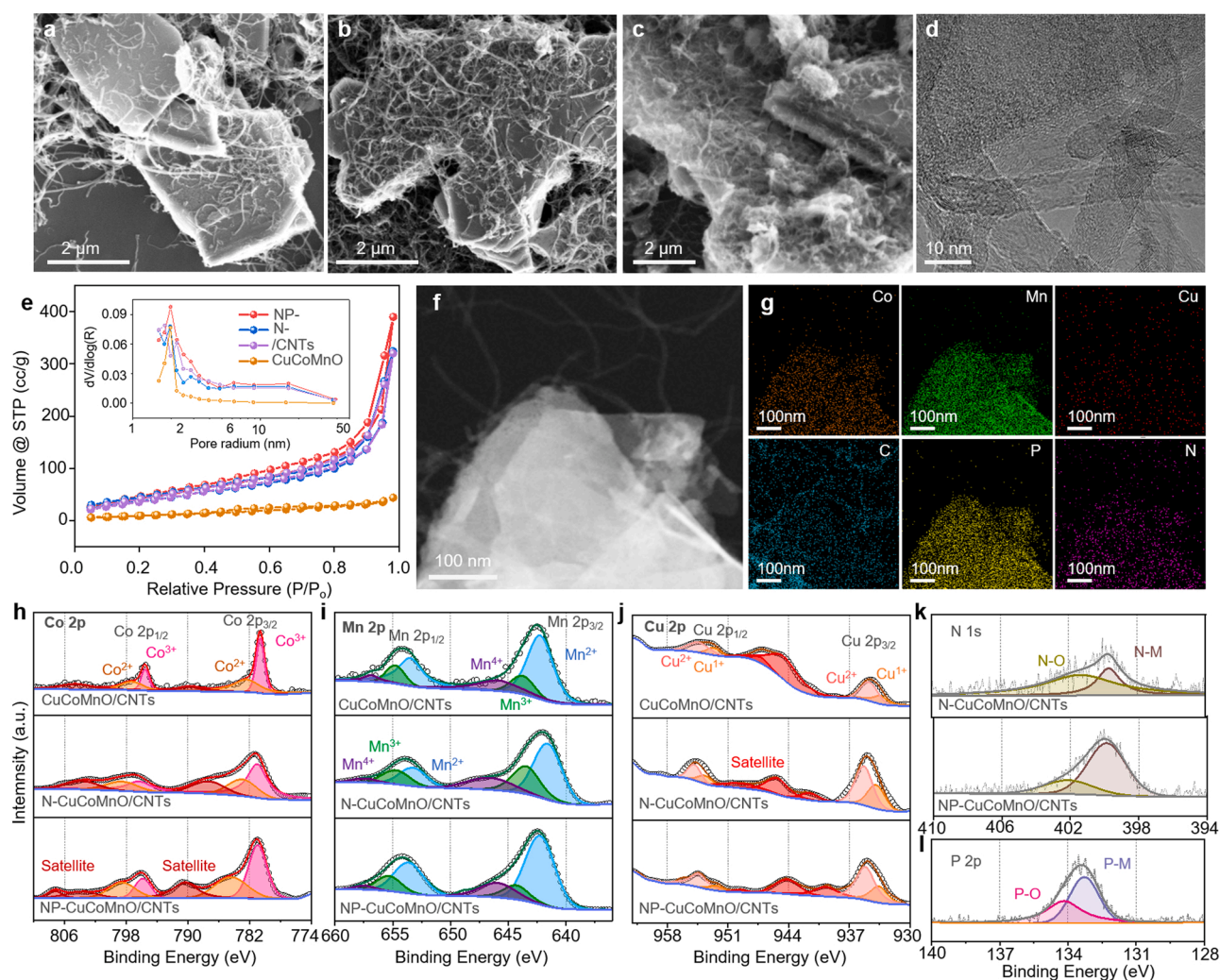
Fig. 2. SEM images of (a) Cu$_{0.1}$Co$_{0.3}$Mn$_{0.6}$O$_2$/CNTs, (b) N-Cu$_{0.1}$Co$_{0.3}$Mn$_{0.6}$O$_2$/CNTs, and (c) P/N-Cu$_{0.1}$Co$_{0.3}$Mn$_{0.6}$O$_2$/CNTs; (d) TEM image of P/N-Cu$_{0.1}$Co$_{0.3}$Mn$_{0.6}$O$_2$/CNTs; (e) N$_2$ sorption isotherms and the size distribution in the inset; (f) HR-TEM image in dark field mode and (g) the corresponding EDS pattern of the elements Co, Mn, Cu, C, P and N; XPS spectra of (h) Co 2p, (i) Cu 2p, (j) Mn 2p, (k) N 1 s, and (l) P 2p.

being exposed on the surface, as shown in Fig. S7. Therefore, they have a much higher chance of being modified by the nonmetallic elements, i.e., P and N, than the oxide particles of the surface, which can further regulate the intrinsic activity of Co/Mn sites. For comparison, two additional controlled samples were synthesized, including $Cu_{0.1}Co_{0.3}Mn_{0.6}O_2$/CNTs without N/P doping, and $Cu_{0.1}Co_{0.3}Mn_{0.6}O_2$/CNTs with only N doping. Noteworthy, P/N co-doped carbon materials under suitable ratios have also demonstrated decent OER/ORR performance [25,27]. However, their intrinsic catalytic performance in this work is not comparable with the metallic oxide nanosheets. Therefore, both the N-doped CNTs and N/P co-doped CNTs were both denoted as CNTs, which are mainly used to improve the electrical conductivity of the catalysts.

According to the SEM of $Cu_{0.1}Co_{0.3}Mn_{0.6}O_2$/CNTs (Fig. 2a), it shows a dense bulk morphology with CNTs evenly embedded in them, which means that the physical dispersion of $Cu_{0.1}Co_{0.3}Mn_{0.6}O_2$ on CNTs cannot effectively impede their restacking due to the strong Van der Waals forces exerted between them. This has also been confirmed by the XRD results in Fig. S8, where the peak corresponding to the layered structure is quite sharp. After N doping (Fig. 2b), the surface becomes fluffy, and a more sheeted area is exposed without aggregation. When N and P are co-doped (Fig. 2c), the 2D nanosheets expose an even larger surface area and wider interspace in-between rather than stacked up, which is beneficial for the access of reactants to or the removal of the products from the active sites. The corresponding high-resolution TEM image (Fig. 2d) indicates that the CNTs are homogeneously distributed on the surface of the N/P co-doped metal oxide nanosheets. The XRD results of N-$Cu_{0.1}Co_{0.3}Mn_{0.6}O_2$/CNTs and N/P-$Cu_{0.1}Co_{0.3}Mn_{0.6}O_2$/CNTs (Fig. S8) show broad and low intensity peaks, further indicating the function of N and P doping to impede the restacking of oxide nanosheets and increase their surface area.

The specific surface area and pore size measurements by the N_2 sorption isotherms further prove the increased surface area and higher porosity of the composites after the N/P doping (Fig. 2e). The N/P-$Cu_{0.1}Co_{0.3}Mn_{0.6}O_2$/CNTs show a mesoporous nature with a pore size in the range of 1–5 nm and a specific surface area of 166.2 $m^2 \cdot g^{-1}$, much larger than that of $Cu_{0.1}Co_{0.3}Mn_{0.6}O_2$ nanosheets (36.5 $m^2 \cdot g^{-1}$) (Fig. S9 and Table S1). From Fig. 2a-c, it can be seen that the CNTs are well mixed with the oxide nanosheets with and without N/P doping. Therefore, the increased surface area of $Cu_{0.1}Co_{0.3}Mn_{0.6}O_2$/CNTs after N and P doping should be due to the reduced Van der Waals forces between the oxide nanosheets, which hinder the restacking of the oxide nanosheets, retaining and enlarging their surface area.

Then, Transmission electron microscopy (TEM) and X-ray photoelectron spectroscopy (XPS) were used to identify the change that happened on the oxide nanosheets after the P/N doping. From the dark field TEM image of the N/P-$Cu_{0.1}Co_{0.3}Mn_{0.6}O_2$/CNTs (Fig. 2f), it is shown that the oxide nanosheets keep the ultrathin sheet morphology and that the CNTs are located between the oxide nanosheets. According to the element mapping in Fig. 2g, the Co, Mn, and Cu elements are uniformly distributed on the surface of the oxide nanosheets. Although the carbon film on the copper grid brings some interference, the distribution of the carbon elements along the CNTs can still be clearly identified. On the other hand, the N and P distributions are mainly overlapped with the metallic element distribution, not with the carbon element distribution, which means that the N and P elements are mainly doped into the metal oxide nanosheets rather than on the surface of the CNTs. The weakened Van der Waals forces between the oxide nanosheets should be ascribed to these doped N and P elements. The replacement of the oxygen atoms with the dopants, especially large-sized P atoms, inside the oxides needs to overcome a big energy barrier for the dopants to diffuse inside the particles, which is the main reason for the rare reports on nonmetallic-element-doped metal oxides. In our case, all the atoms of the oxide nanosheets are exposed on the surface, and the lattice replacement of the oxygen atoms with heteroatoms hinders the diffusion process of the heteroatom, which is

generally easy. In addition, the heteroatoms can also locate on the surface of the nanosheets to form bonds with the metallic and oxygen atoms. Therefore, the N/P elements can genuinely be doped into the oxide nanosheets [48].

According to the XPS results, with the introduction of the P elements (1.8 at%), the content of the doped N atoms increased from 2.7 at% to 4.7 at%, which is similar with previous reports on the N/P co-doping, suggesting that the P element makes more defects on the catalysts and increases the content of the N elements inside the nanosheet [27].

The narrow scan spectra of the different elements, i.e., Co, Mn, Cu, N, and P, were used to identify the bond structure change after the P/N doping. From Fig. 2h-l, it can be seen that the addition of N and P atoms didn't bring additional peaks on the spectra corresponding to the transition metals, i.e., Co, Mn, and Cu. In the meantime, the main peak position slightly shifts after the N and P doping, but the ratio of each peak changes in contrast to the Cu doping inside the in-plane structure of the oxide nanosheets. These results indicate that the N and P atoms don't change the conduction band formed by the metallic atoms but mainly influence the valence band constructed by the oxygen atoms. However, with the tuning of the electronic structure by the nonmetallic atoms (N, P), the Co^{3+}/Co^{2+} and Mn^{3+}/Mn^{2+} ratios increase (Table S2), which will further help the adsorption of OH^- on the Co sites and the desorption of OH^- on the Mn sites, consequently having a big influence on the performance of OER and ORR [50]. With the N/P co-doping, this change is more apparent than only with the N doping, which should be due to the increased content of N inside the framework with the help of P atoms (Fig. 2k). On the other hand, we notice that the ratio of the N-M (M=Co, Mn, Cu, 399.1 eV) bonds to the N-O (402.5 eV) bonds also greatly increases from ~1:1–4:1 with the P doping (Table S2). This fact indicates that the P elements increase the replacement degree of the lattice O atoms with N atoms to form N-M bonds rather than bind the N atoms on the surface of the nanosheets with the M/O atoms. From the P 2p spectrum (Fig. 2l), we find that the ratio of the P-O bonds (134.2 eV) to the P-M bonds (133.0 eV) is around 1:1, which means that the P elements are mainly located on the surface of the sheets to form P-M and P-O bonds (Table S2).

The above bond structure analysis indicates the high concentration of the nonmetallic elements doped inside the oxide nanosheets and the great modulation introduced to the coordination environment of the metal catalytic sites (Co, Mn atoms). According to the literature, small amounts of nonmetallic elements modified on the surface of metal oxides can greatly enhance the performance of catalysts [50–54]. Therefore, the as-prepared N/P-$Co_{0.3}Mn_{0.6}Cu_{0.1}O_2$ six-element nanosheets with a high concentration of Cu, P, and N dopants should show good oxygen-related electrocatalytic performance.

3.3. OER performance

To understand the influence of the triple-element (Cu, N, P) doping on the electrocatalytic performance of the $Co_{0.4}Mn_{0.6}O_2$ nanosheets, the OER activity of all the catalysts was examined using a three-electrode configuration in a 1.0 M KOH alkaline solution. Firstly, the LSV polarization curves were measured to obtain the overpotential and Tafel slope values for all the samples, both of which are important to evaluate the OER performance (Fig. 3a-c).

The measured potentials vs. Ag/AgCl were converted to the reversible hydrogen electrode (RHE) scale according to the Nernst equation: $E_{RHE} = E_{Ag/AgCl} + 0.0591 \text{ pH} + E_{Ag/AgCl}$. Where E_{RHE} is the converted potential vs. RHE, $E°_{Ag/AgCl} = 0.1976$ at 25 °C, $E_{Ag/AgCl}$ is the experimentally measured potential against Ag/AgCl reference, and in the present case pH= 14.

The $Co_{0.4}Mn_{0.6}O_2$ and $Cu_{0.1}Co_{0.3}Mn_{0.6}O_2$ nanosheets display ultra-low electrocatalytic activity due to their poor electrical conductivity (Fig. 3c). After the addition of CNTs, the OER activity is remarkably enhanced. Compared with the $Co_{0.4}Mn_{0.6}O_2$/CNTs, the $Cu_{0.1}Co_{0.3}Mn_{0.6}O_2$/CNTs composite shows a much better OER
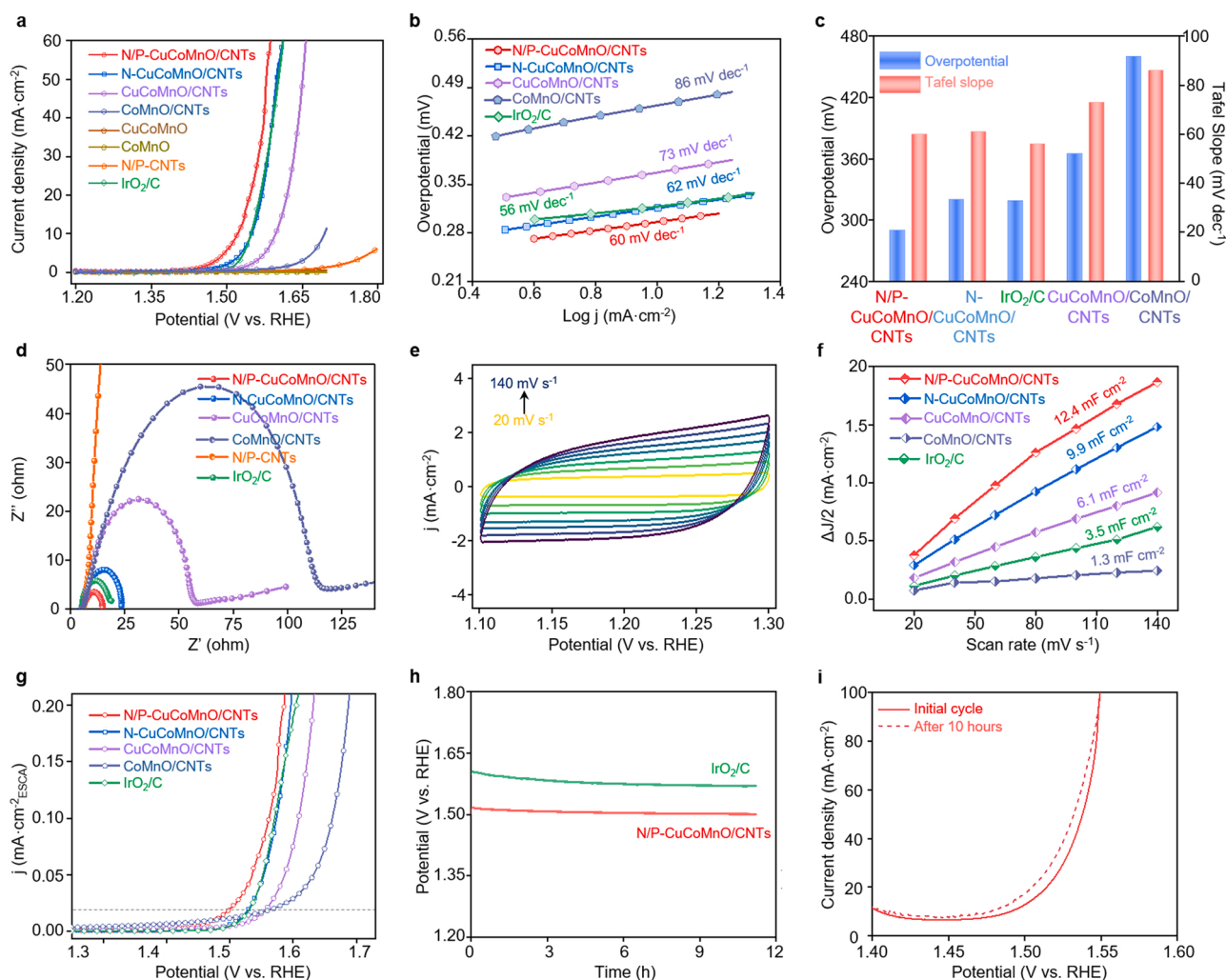
Fig. 3. The OER electrocatalytic performance in 1.0 M KOH; (a) LSV curves of OER at a scan rate of 5 mV s^{-1}; (b) The corresponding Tafel slopes; (c) Comparison of the overpotential at 10 mA cm^{-2} and Tafel slopes; (d) The Nyquist plot of EIS measured at the overpotential of 290 mV; (e) CVs in the potential window of 1.1–1.3 V vs RHE at scan rates from 20 mV s^{-1} to 140 mV s^{-1} for N/P-Cu$_{0.1}$Co$_{0.3}$Mn$_{0.6}$O$_2$/CNTs; (f) The capacitive current density as a function of the scan rate; (g) The electrochemically active surface area (ECSA) normalized linear-sweep voltammetry (LSV) curves; (h) The galvanostatic stability test at a constant current density of 10 mA cm^{-2} for 10 h; (i) The polarization curves before and after 10 h's aging test.

performance. For instance, it shows an overpotential (η_{10}) of 366 mV to deliver a current density of 10 mA cm^{-2}, much lower than the Co$_{0.4}$Mn$_{0.6}$O$_2$/CNTs (463 mV). This result confirms the great positive effect of the Cu doping to activate the Co catalytic sites in the Co$_{0.4}$Mn$_{0.6}$O$_2$.

After the post-doping of N and P into the Cu$_{0.1}$Co$_{0.3}$Mn$_{0.6}$O$_2$ nanosheets, the η_{10} value is further reduced to 319 mV and 290 mV for the N-Cu$_{0.1}$Co$_{0.3}$Mn$_{0.6}$O$_2$/CNTs and N/P-Cu$_{0.1}$Co$_{0.3}$Mn$_{0.6}$O$_2$/CNTs, respectively, which are lower than the value for IrO$_2$ (320 mV) (Fig. 3c). Compared with the literature reported bimetallic transition metal oxides for OER, the performance of N/P-Cu$_{0.1}$Co$_{0.3}$Mn$_{0.6}$O$_2$/CNTs is still superior (Table S3). The LSV curves have also been studied with different counter and reference combinations, which showed very small performances difference (Fig. S10), indicating the accuracy of the as obtained results [55]. In addition, the performance of N/P-Cu$_{0.1}$Co$_{0.3}$Mn$_{0.6}$O$_2$ and N- Cu$_{0.1}$Co$_{0.3}$Mn$_{0.6}$O$_2$ without addition of CNTs were also provided in Fig. S11. According to the LSV curve, the N/P-doped CNTs show negligible OER activity, which means that the CNTs only increase the electrical conductivity. Therefore, the enhanced performance is mainly ascribed to the N/P dopants inside the oxide nanosheets. In other words, the three doped elements (Cu, N, P) inside the Co$_{0.4}$Mn$_{0.6}$O$_2$ nanosheets can gradually increase the activity of the Co$_{0.4}$Mn$_{0.6}$O$_2$/CNTs for OER.

The Tafel slope reflects the reaction kinetics of a catalyst, where smaller values represent faster dynamics. The Tafel slope value for IrO$_2$, Co$_{0.4}$Mn$_{0.6}$O$_2$/CNTs, Cu$_{0.1}$Co$_{0.3}$Mn$_{0.6}$O$_2$/CNTs, N-Cu$_{0.1}$Co$_{0.3}$Mn$_{0.6}$O$_2$/CNTs, and N/P-Cu$_{0.1}$Co$_{0.3}$Mn$_{0.6}$O$_2$/CNTs is 56 mV dec^{-1}, 86 mV dec^{-1}, 73 mV dec^{-1}, 61 mV dec^{-1}, and 60 mV dec^{-1}, respectively (Fig. 3c). It means that the reaction kinetics gradually increase with the gradual doping of the three elements (Cu, N, P) inside the Co$_{0.4}$Mn$_{0.6}$O$_2$. The Tafel slope is influenced by the charge transfer at the electrode/electrolyte interface.

To uncover the mechanism for the decreased Tafel slope with the doping of Cu, N, P elements, we firstly used electrochemical impedance spectroscopy (EIS) to analyze the charge transfer at the interface. The Nyquist plots for all samples were obtained at 1.52 V (vs. RHE). As seen from Fig. 3d, the charge transfer resistance (R_{ct}) for IrO$_2$/C, Co$_{0.4}$Mn$_{0.6}$O$_2$/CNTs, Cu$_{0.1}$Co$_{0.3}$Mn$_{0.6}$O$_2$/CNTs, N-Cu$_{0.1}$Co$_{0.3}$Mn$_{0.6}$O$_2$/CNTs, and N/P-Cu$_{0.1}$Co$_{0.3}$Mn$_{0.6}$O$_2$/CNTs is 13.7 Ω, 111.7 Ω, 52.5 Ω, 18.4 Ω, and 9.6 Ω, respectively. This result means that the sequential doping has gradually increased the charge transfer speed at the electrode surface. Based on the SEM images and BET results, this result should be ascribed to the increased surface area of the composites after the Cu, N, P doping into the oxide nanosheets, which sidesteps the restacking of the oxide nanosheets.

Secondly, the ECSAs were evaluated. The cyclic voltammetry (CV) curves in the non-faradic region (1.1–1.3 V vs RHE) at different scanning rates (20–140 mV s^{-1}) were measured (Figs. 3e and S12). The linear fit of the current change (ΔJ) at 1.2 V (vs RHE) from the CV curves as a function of the scan rate was used to calculate the double-layer capacitance (C_{dl}) (Fig. 3f). The as-obtained C_{dl} value for $Co_{0.4}Mn_{0.6}O_2$/CNTs, $Cu_{0.1}Co_{0.3}Mn_{0.6}O_2$/CNTs, N-$Cu_{0.1}Co_{0.3}Mn_{0.6}O_2$/CNTs, and N/P-$Cu_{0.1}Co_{0.3}Mn_{0.6}O_2$/CNTs is 1.3 mF cm^{-2}, 6.1 mF cm^{-2}, 9.9 mF cm^{-2}, and 12.4 mF cm^{-2}, respectively (Table S4). These capacitances correspond to an ECSA of 6.4 cm^2, 29.9 cm^2, 48.5 cm^2, and 60.8 cm^2, respectively. These results indicate that the dopants gradually increase the ECSA of the $Co_{0.4}Mn_{0.6}O_2$/CNTs due to the reduced Van der Waals force between the oxide nanosheets to impede their restacking and expose more active sites on the surface, consistent with the physical characterizations by SEM and BET. Therefore, the smaller Tafel slope in N/P-$Cu_{0.1}Co_{0.3}Mn_{0.6}O_2$/CNTs is ascribed to both the quicker charge transfer in the electrodes and the larger ECSA.

To exclude the interference of the catalytic site number to evaluate the intrinsic activity of each Co site, we normalized the LSV curves in Fig. 3a by their ECSA (Fig. 3g). At an overpotential of 350 mV, the current density for $Co_{0.4}Mn_{0.6}O_2$/CNTs, $Cu_{0.1}Co_{0.3}Mn_{0.6}O_2$/CNTs, N-$Cu_{0.1}Co_{0.3}Mn_{0.6}O_2$/CNTs, N/P-$Cu_{0.1}Co_{0.3}Mn_{0.6}O_2$/CNTs, and IrO_2/C is 0.07 mA cm$_{ECSA}^{-2}$, 0.12 mA cm$_{ECSA}^{-2}$, 0.36 mA cm$_{ECSA}^{-2}$, and 0.55 mA cm$_{ECSA}^{-2}$ and 0.39 mA cm$_{ECSA}^{-2}$, respectively. The gradual increase of the ECSA normalized current density indicates that each doping element increases the activity of the Co sites for OER. The Co site with triple-dopant modulation shows an activity better than the Ir site in the IrO_2. Therefore, based on the above discussion, the triple dopants can promote the OER performance by promoting the intrinsic activity of the Co site, increasing the surface area of the composites, and facilitating the mass transfer during the reaction process.

The turnover frequency (TOF) was calculated to further gain a quantitative insight into the intrinsic catalytic activity (Fig. S13 and Table S5). The concentration of active sites in the catalyst (Ns) values of N/P-$Cu_{0.1}Co_{0.3}Mn_{0.6}O_2$/CNTs, N-$Cu_{0.1}Co_{0.3}Mn_{0.6}O_2$/CNTs and $Cu_{0.1}Co_{0.3}Mn_{0.6}O_2$/CNTs were calculated to be 6.77×10^{-8}, 2.97×10^{-8}, 1.33×10^{-8} mol cm^{-2}, respectively. The TOF values for N/P-$Cu_{0.1}Co_{0.3}Mn_{0.6}O_2$/CNTs at the potential of 1.60 V were estimated to be 6.85×10^{-2} s^{-1}, which was larger than that of N-$Cu_{0.1}Co_{0.3}Mn_{0.6}O_2$/CNTs ($6.35 \times 10^{-2}$ s^{-1}) and $Cu_{0.1}Co_{0.3}Mn_{0.6}O_2$/CNTs ($3.20 \times 10^{-2}$ s^{-1}), respectively. These results indicate that the catalysts doped N, P atoms show a good oxygen-related electrocatalytic performance. The dopant of N and P atoms into $Cu_{0.1}Co_{0.3}Mn_{0.6}O_2$ increased the concentration of catalytic sites twice, and significantly enhanced the intrinsic activity of Co based catalytic sites.

To evaluate the OER stability of the optimized N/P-$Cu_{0.1}Co_{0.3}Mn_{0.6}O_2$/CNTs catalysts, a long-term chronopotentiometry test at a current density of 10 mA cm^{-2} was carried out with the commercial IrO_2/C as a comparison (Fig. 3h). The N/P-$Cu_{0.1}Co_{0.3}Mn_{0.6}O_2$/CNTs sample maintains an overpotential of ~290 mV for over 10 h. In contrast, the IrO_2/C shows an overpotential change from 390 mV to 340 mV after a 10 h stability test. After the stability test, the LSV curve for N/P-$Cu_{0.1}Co_{0.3}Mn_{0.6}O_2$/CNTs showed a negligible change, with a slight η_{10} value decrease by 10 mV (Fig. 3i). Based on the post-electrolysis characterization, as seen from Figs. S14-15, the catalysts shown well stability with preserving initial morphology and similar composition to the original sample. Therefore, the triple-element-doped N/P-$Cu_{0.1}Co_{0.3}Mn_{0.6}O_2$/CNTs show both superior OER activity and stability.

3.4. Theoretical calculations

To rationalize the utmost enhancement in the OER activity for the overhead doping elements (Cu, N, P) on the $Co_{0.4}Mn_{0.6}O_2$ nanosheet, we
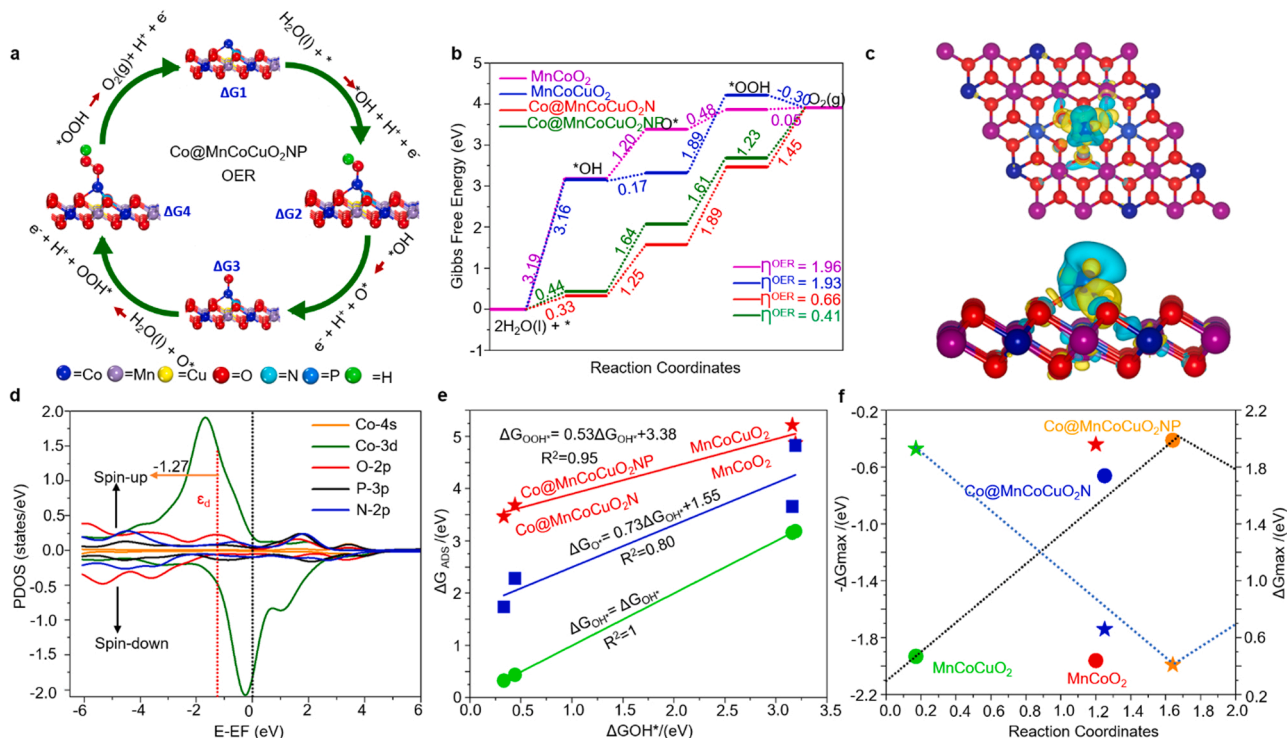
Fig. 4. (a) Schematic illustration of the 4e$^-$ OER pathway on the active site of doped $Co_{0.4}Mn_{0.6}O_2$ nanosheets with the optimized configurations for the intermediates; (b) The potential free energy profiles of the intermediate states in OER on $Co_{0.4}Mn_{0.6}O_2$, $Cu_{0.1}Co_{0.3}Mn_{0.6}O_2$, $Cu_{0.1}Co_{0.3}Mn_{0.6}O_{1.8}N_{0.2}$, and $Cu_{0.1}Co_{0.3}Mn_{0.6}O_{1.8}N_{0.2}P_{0.2}$ nanosheets at zero potentials; (c) CDD of the $Cu_{0.1}Co_{0.3}Mn_{0.6}O_{1.8}N_{0.2}P_{0.2}$ nanosheets, where the yellow (cyan) iso-surface indicates charge accumulation (depletion) regions. The contour iso-value of the CDD is $\pm$ 0.05 a.u; (d) The PDOS projected on the Co 3d (green), O 2p (red), N 2p (blue), and P 3p (black) states. The Fermi level is set to zero; (e) Scaling relationship between the Gibbs free energy (ΔG) and the oxygenated (ΔG_{OH^*}, ΔG_{O^*}, and ΔG_{OOH^*}) intermediates; (f) In order to display the OER activity trend, the $\Delta G_{O^*} - \Delta G_{OH^*}$ step is plotted vs the negative maximum potential-limiting ($-\Delta G_{max}$) step.

conducted first principles calculations (Fig. 4 and Figs. S16-S23). Generally, the entire OER process in alkaline media comprises four elementary electron steps, with *OH, *O, *OOH, and O_2 as the intermediate products (Figs. 4a and S16-S19) [53–56]. These intermediates were adsorbed on the surface of catalyst models (Fig. S19), i.e., $Co_{0.4}Mn_{0.6}O_2$, $Cu_{0.1}Co_{0.3}Mn_{0.6}O_2$, $Cu_{0.1}Co_{0.3}Mn_{0.6}O_{1.8}N_{0.2}$, and $Cu_{0.1}Co_{0.3}Mn_{0.6}O_{1.8}N_{0.2}P_{0.2}$. The bond structures for these four nanosheets are based on the XRD and XPS analysis, where it was shown that the $Co_{0.4}Mn_{0.6}O_2$ and $Cu_{0.1}Co_{0.3}Mn_{0.6}O_2$ inherit the in-plane structure from their layered precursor. The N atoms are bonded to the Co atoms to activate them from the in-plane structure, and the P atoms are also bonded with the Co atoms and oxygen atoms to further modulate the Co electronic structure (Fig. S19). Fig. 4b shows that all the elementary steps of the OER for the selected systems are uphill in the PEP (Potential Energy Profile) at the zero potential (U = 0 V). Based on the potential energy diagram for each step, the corresponding overpotential (η^{OER}) value for each model can be calculated from the Eq. (S6) (see experimental section).

From the potential energy diagram (Fig. 4b), we found that the formation of $*H_2O \rightarrow *OH + *H$ radical on the $Co_{0.4}Mn_{0.6}O_2$ and $Cu_{0.1}Co_{0.3}Mn_{0.6}O_2$ nanosheets is the rate-determining step (RDS) for the OER due to the largest ΔG value. The calculated overpotentials are 1.96 and 1.93 V for the $Co_{0.4}Mn_{0.6}O_2$ and $Cu_{0.1}Co_{0.3}Mn_{0.6}O_2$, respectively. On the other hand, the adsorption energy of the OH radicals are significantly reduced after the N doping and N/P co-doping inside the oxide nanosheets. In the case of the $Cu_{0.1}Co_{0.3}Mn_{0.6}O_{1.8}N_{0.2}$ system, the third step was found to be the RDS, where the remaining atomic *O species react with the second H_2O molecule to form the *OOH species, and the corresponding overpotential is 0.66 V. However, for the $Cu_{0.1}Co_{0.3}Mn_{0.6}O_{1.8}N_{0.2}P_{0.2}$ system, the second step was found to be RDS, where the *OH radical dissociates into *O and *H species, and the calculated overpotential is 0.41 V. The lowest overpotential (0.41 V) compared with the other catalyst models indicates the best OER activity for $Cu_{0.1}Co_{0.3}Mn_{0.6}O_{1.8}N_{0.2}P_{0.2}$ nanosheets. All these results imply that all the dopants (Cu, N, P) play an important role in reducing the energy barrier of the oxide nanosheets and improving the OER performance, which is consistent with experimental results in Fig. 3a. These results show the same trend as the experimental ones, but the overpotential values show large deviations from the experimental data. The main reason should be that the DFT analysis does not consider the concentration of the different dopants.

To further understand the enhanced catalytic activity of the selected models, the charge density difference (CDD) was calculated. The CDD is presented in Figs. 4c and S21. The apparent change in the charge distribution can be clearly identified after the sequential doping, where the yellow and cyan colors represent the charge accumulation and depletion regions, respectively. Fig. 4c shows that the charge density flows from the Co atom towards the neighboring doped N, P, and O atoms. According to the Bader charge analysis, the Co atoms is + 0.86 |e|, indicating a considerable charge transfer from the Co atom to the surface. It is concluded that the charge transfer between the Co and surface is primarily liable for the robust binding and formation of chemical bonds. Meanwhile, the positive charge of the Co atom stabilizes the oxygenated intermediates (*O, *OH, *OOH and $*O_2$) during the catalytic process. The result of the Bader charge analysis is in good agreement with the CDD assessment, indicating that the charge transfer between the catalytic sites and the surface facilitates the OER.

In order to investigate the doping effect on the $Co_{0.4}Mn_{0.6}O_2$ nanosheets, we calculated the partial density of state (PDOS) on the d and s orbitals of the metal atoms' (M= Co, Mn, Cu) and adjacent atoms' X (X = O, N, P) orbitals. As described in Figs. 4d and S22 the s and d orbitals of the metal atoms are strongly hybridized with the p orbitals of the doped atoms at the active site near the Fermi level (E_F). Moreover, the presence of the 3d orbital of the Co atom close to the E_F shows high reactivity, which can activate the intermediates during the catalytic process. As shown in Fig. 4d, the calculated D-band center of Co (Co 3d)

is − 1.27 eV, close to the energy position for the transformation from *OOH to O_2. Therefore, the doping-induced shifts in the d-band-center play a significant role in enhancing the OER activity, which greatly increases the PDOS of Co 3d around the theoretical OER energy position [57–59]. The d-band centers move to the left side of the Fermi level when the d-electron occupation rises, and the interaction among the Co atom and the intermediates (*OH, *O, *OOH) become weaker (see Fig. S23). As a result, in comparison to the other examined systems, the overpotential of OER for $Cu_{0.1}Co_{0.3}Mn_{0.6}O_{1.8}N_{0.2}P_{0.2}$ become relatively lower. The admirable OER activity of the doped $Co_{0.4}Mn_{0.6}O_2$ nanosheets is further clarified by a description of the binding force between the intermediates and the active centers. The Gibbs free energies of the oxygenated (ΔG_{OH^*}, ΔG_{O^*}, and ΔG_{OOH^*}) intermediates can be used to evaluate the OER activity.

The descriptor-based method [60] can efficiently recognize and enterprise the most suitable systems if the adsorption energies of these intermediates are interrelated. For the doped $Co_{0.4}Mn_{0.6}O_2$ nanosheets, Fig. 4e illustrates the correlation between the oxygenated (ΔG_{OH^*}, ΔG_{O^*}, and ΔG_{OOH^*}) intermediates and the adsorption free energy. Regardless of the active center, we found a universal scaling relation between ΔG_{OH^*} and ΔG_{OOH^*}. ΔG_{OOH^*} can be specified (Fig. 4e) as a function of ΔG_{OH^*} by $\Delta G_{OOH^*} = 0.53\Delta G_{OH^*} + 3.38$. The coefficient of determination (R^2) is 0.95, indicating that ΔG_{OOH^*} and ΔG_{OH^*} have a strong linear relationship. On the other hand, a relationship between the adsorption energies of ΔG_{OH^*} and ΔG_{O^*} appears to be less likely. As a result, the energy difference of $\Delta G_{O^*} - \Delta G_{OH^*}$ is a unique descriptor for the OER performance. For the doped $Co_{0.4}Mn_{0.6}O_2$ systems, the relationship between $\Delta G_{O^*} - \Delta G_{OH^*}$ and the negative maximum potential-limiting step was further explored.

The volcano curve correlation between the negative maximum potential-limiting steps and $\Delta G_{O^*} - \Delta G_{OH^*}$ is shown in Fig. 4f. The $Cu_{0.1}Co_{0.3}Mn_{0.6}O_{1.8}N_{0.2}P_{0.2}$ has the lowest η^{OER} values (0.41), which is close to the peak position of the volcano curve among the other configurations. As a result, the $Cu_{0.1}Co_{0.3}Mn_{0.6}O_{1.8}N_{0.2}P_{0.2}$ nanosheets are promising for OER, as confirmed by the electrochemical characterizations.

3.5. Zinc-air battery performance

The ORR performance of the samples was also studied in 1.0 M KOH (Fig. S24). The N/P-$Cu_{0.1}Co_{0.3}Mn_{0.6}O_2$/CNTs show a half-wave potential $E_{1/2}$ of 0.82 V (vs RHE), only slightly poorer than the 0.87 V of Pt/C, confirming its high catalytic activity for ORR. Then, we used co-doped optimized OER/ORR bifunctional catalyst in a Zn-air battery (ZAB) application with a Zn foil as an anode (Fig. 5a, b).

The IrO_2-Pt/C-based ZAB was also prepared for comparison. As seen from Fig. 5c, the N/P-$Cu_{0.1}Co_{0.3}Mn_{0.6}O_2$/CNTs-based ZAB delivers an open circuit potential of 1.46 V for over 30 h, higher than the value of 1.38 V for the IrO_2-Pt/C-based ZAB. Fig. 5d compares the discharge curves and the corresponding power density curves of the two ZABs. The N/P-$Cu_{0.1}Co_{0.3}Mn_{0.6}O_2$/CNT-based ZAB displays a peak power density of 108.1 mW cm^{-2}, slightly higher than the 103.3 mW cm^{-2} for the IrO_2-Pt/C. In the meantime, the discharge and charge curves of the N/P-$Cu_{0.1}Co_{0.3}Mn_{0.6}O_2$/CNTs-based ZAB shows a smaller voltage gap at the high current density range (100–300 mA cm^{-2}) than that of the IrO_2-Pt/C-based ZAB, which should be ascribed to the good stability of our oxide-based catalysts at high current densities (Fig. 5e). The better stability of our N/P-$Cu_{0.1}Co_{0.3}Mn_{0.6}O_2$/CNTs than the noble metal-based IrO_2-Pt/C was further demonstrated by cycling the two ZABs at 10 mA cm^{-2} (Fig. 5f).

According to the charge/discharge voltage profiles in Fig. 5g, the voltage gap of the N/P-$Cu_{0.1}Co_{0.3}Mn_{0.6}O_2$/CNTs-based ZABs displays an initial value of 0.99 V and increases merely by 0.25 V after 200 h operation. In contrast, the voltage gap for the IrO_2-Pt/C-based ZABs increases rapidly from 1.24 V to 1.96 V after only 60 h operation. The LED light can be successfully powered by the two sets of connected N/P-
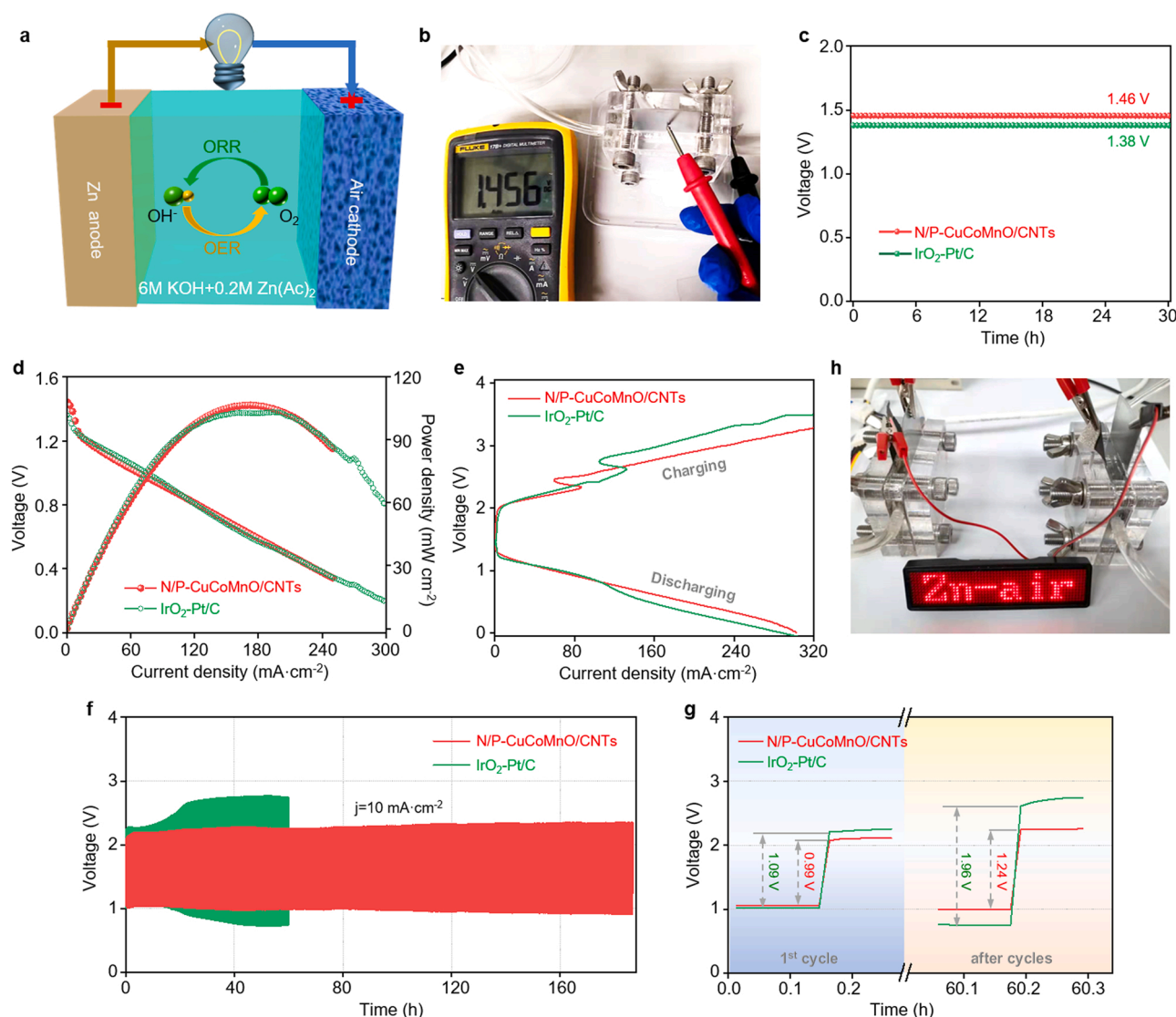
Fig. 5. Electrochemical performance of the Zn-air battery: (a) schematic illustration of the rechargeable Zn−air battery; (b) Digital photo of the open-circuit potential; (c) The open circuit voltage curves for 30 h; (d) The power density and discharge curves using N/P-$Cu_{0.1}Co_{0.3}Mn_{0.6}O_2$/CNTs and IrO_2-Pt/C as cathodes; (e) The charge and discharge curves; (f) The cycling performance at 10 mA·cm^{-2}; (g) The difference of the voltage plateaus during charge and discharge for the first and last cycles; (h) Digital photo of the LED lamp powered by two connected zinc-air batteries.

$Cu_{0.1}Co_{0.3}Mn_{0.6}O_2$/CNTs-based ZABs (Fig. 5 h). In all, the N/P-$Cu_{0.1}Co_{0.3}Mn_{0.6}O_2$/CNTs-based ZABs show superior comprehensive performance than the IrO_2-Pt/C-based ZABs.

4. Conclusions

We developed a strategy to effectively dope multiple heteroatoms into bimetallic transition metal oxides by fabricating these oxides into uni-lamellar oxide nanosheets ($Co_{0.4}Mn_{0.6}O_2$). The heteroatoms (Cu, N, P) can be genuinely and heavily doped inside these nanosheets either through an mixing doping and post-doping strategy. Due to the full exposure of the Co/Mn metallic sites on the surface of the nanosheets, the dopants largely modulated the bonding environment of the catalytic sites. Through electrochemical and DFT characterizations, we found that these dopants (Cu, N, P) facilitate the charge transfer at the electrode/electrolyte interface and increase the ESCA and the intrinsic activity of the catalytic Co/Mn sites. As such, these dopants greatly enhance the OER/ORR performance of $Co_{0.4}Mn_{0.6}O_2$. The triple-element-doped catalyst, N/P-$Cu_{0.1}Co_{0.3}Mn_{0.6}O_2$/CNTs, shows an overpotential (η_{10}) of 290 mV and a Tafel slope of 60 mV dec^{-1} for OER, much better than the $Co_{0.4}Mn_{0.6}O_2$/CNTs (463 mV, 86 mV dec^{-1}). Moreover, these dopants also improve the ORR performance of the $Co_{0.4}Mn_{0.6}O_2$/CNTs composites. By applying the N/P-$Cu_{0.1}Co_{0.3}Mn_{0.6}O_2$/CNTs as a bifunctional catalyst for ZAB, we display a slightly higher peak power density and larger open circuit voltage than the IrO_2-Pt/C-based ZAB. Moreover, the good cycling stability for the transition metal oxides is preserved after the heavy doping of the three elements. Generally, the mediocre OER and ORR performance of the bimetallic transition metal oxides hinder their applications. We envision that the strategy in this work, i.e., fabricating bimetallic transition metal oxides into uni-lamellar sheets and then heavily doping them with heteroatoms, should provide a guideline to develop low-cost but high-performance catalysts for ZAB applications.

CRediT authorship contribution statement

Ying Li: Conceptualization, Methodology, Investigation, Data curation. **Shamraiz Hussain Talib:** Investigation, Validation, Writing − original draft. **Dongqing Liu:** Validation, Data curation, Writing − original draft. **Kai Zong:** Methodology, Validation. **Ali Saad:** Validation,

Data curation, Visualization. **Zhaoqi Song:** Methodology, Investigation. **Jie Zhao:** Formal analysis, Visualization, Data curation. **Wei Liu:** Methodology, Investigation, Formal analysis. **Fude Liu:** Methodology, Investigation, Writing − original draft. **Qianqian Ji:** Validation, Data curation. **Panagiotis Tsiakaras**: Conceptualization, Methodology, Writing − review & editing. **Xingke Cai:** Conceptualization, Supervision, Project administration, Funding acquisition, Writing − review & editing.

Declaration of Competing Interest

The authors declare that they have no known competing financial interests or personal relationships that could have appeared to influence the work reported in this paper.

Data availability

Data will be made available on request.

Acknowledgments

Appendix A. Supporting information

Supplementary data associated with this article can be found in the online version at doi:10.1016/j.apcatb.2022.122023.

References

[1] S. Ghosh, R.N. Basu, Multifunctional nanostructured electrocatalysts for energy conversion and storage: current status and perspectives, Nanoscale 10 (2018) 11241–11280, https://doi.org/10.1039/C8NR01032C.

[2] Q. Liu, Z. Pan, E. Wang, L. An, G. Sun, Aqueous metal-air batteries: fundamentals and applications, Energy Storage Mater. 27 (2020) 478–505, https://doi.org/10.1016/j.ensm.2019.12.011.

[3] R. Yang, Y. Zhou, Y. Xing, D. Li, D. Jiang, M. Chen, W. Shi, S. Yuan, Synergistic coupling of CoFe-LDH arrays with NiFe-LDH nanosheet for highly efficient overall water splitting in alkaline media, Appl. Catal. B 253 (2019) 131–139, https://doi.org/10.1016/j.apcatb.2019.04.054.

[4] J. Fu, Z.P. Cano, M.G. Park, A. Yu, M. Fowler, Z. Chen, Electrically Rechargeable Zinc–Air Batteries: Progress, Challenges, and Perspectives, Adv. Mater. 29 (2017) 1604685, https://doi.org/10.1002/adma.201604685.

[5] D.U. Lee, P. Xu, Z.P. Cano, A.G. Kashkooli, M.G. Park, Z. Chen, Recent progress and perspectives on bi-functional oxygen electrocatalysts for advanced rechargeable metal–air batteries,J, Mater. Chem. A 4 (2016) 7107–7134, https://doi.org/10.1039/C6TA00173D.

[6] K. Song, Y. Feng, X. Zhou, T. Qin, X. Zou, Y. Qi, Z. Chen, J. Rao, Z. Wang, N. Yue, X. Ge, W. Zhang, W. Zheng, Exploiting the trade-offs of electron transfer in MOF-derived single Zn/Co atomic couples for performance-enhanced zinc-air battery, Appl. Catal. B 316 (2022), 121591, https://doi.org/10.1016/j.apcatb.2022.121591.

[7] D. Liu, A. Barbar, T. Najam, M.S. Javed, J. Shen, P. Tsiakaras, X. Cai, Single noble metal atoms doped 2D materials for catalysis, Appl. Catal. B 297 (2021) 120389, https://doi.org/10.1016/j.apcatb.2021.120389.

[8] X. Wu, C. Tang, Y. Cheng, X. Min, S.P. Jiang, S. Wang, Bifunctional catalysts for reversible oxygen evolution reaction and oxygen reduction reaction, Chem. Eur. J. 26 (2020) 3906–3929, https://doi.org/10.1002/chem.201905346.

[9] C.-X. Zhao, J.-N. Liu, J. Wang, D. Ren, B.-Q. Li, Q. Zhang, Recent advances of noble-metal-free bifunctional oxygen reduction and evolution electrocatalysts, Chem. Rev. 50 (2021) 7745–7778, https://doi.org/10.1039/D1CS00135C.

[10] E. Davari, D.G. Ivey, Bifunctional electrocatalysts for Zn–air batteries, Sustain. Energy Fuels 2 (2018) 39–67, https://doi.org/10.1039/C7SE00413C.

[11] C. Hu, L. Dai, Doping of carbon materials for metal-free electrocatalysis, Adv. Mater. 31 (2019) 1804672, https://doi.org/10.1002/adma.201804672.

[12] S. Ren, X. Duan, S. Liang, M. Zhang, H. Zheng, Bifunctional electrocatalysts for Zn–air batteries: recent developments and future perspectives, J. Mater. Chem. A 8 (2020) 6144–6182, https://doi.org/10.1039/C9TA14231B.

[13] W.T. Hong, M. Risch, K.A. Stoerzinger, A. Grimaud, J. Suntivich, Y. Shao-Horn, Toward the rational design of non-precious transition metal oxides for oxygen electrocatalysis, Energy Environ. Sci. 8 (2015) 1404–1427, https://doi.org/10.1039/C4EE03869J.

[14] C.-X. Zhao, H.-F. Wang, B.-Q. Li, Q. Zhang, Multianion transition metal compounds: synthesis, regulation, and electrocatalytic applications, Acc. Mater. Res. 2 (2021) 1082–1092, https://doi.org/10.1021/accountsmr.1c00136.

[15] S. Li, X. Hao, A. Abudula, G. Guan, Nanostructured Co-based bifunctional electrocatalysts for energy conversion and storage: current status and perspectives, J. Mater. Chem. A 7 (2019) 18674–18707, https://doi.org/10.1039/C9TA04949E.

[16] C. Fan, X. Wu, M. Li, X. Wang, Y. Zhu, G. Fu, T. Ma, Y. Tang, Surface chemical reconstruction of hierarchical hollow inverse-spinel manganese cobalt oxide boosting oxygen evolution reaction, Chem. Eng. J. 431 (2022), 133829, https://doi.org/10.1016/j.cej.2021.133829.

[17] Y. Meng, J.-C. Li, S.-Y. Zhao, C. Shi, X.-Q. Li, L. Zhang, P.-X. Hou, C. Liu, H.-M. Cheng, Fluorination-assisted preparation of self-supporting single-atom Fe-N-doped single-wall carbon nanotube film as bifunctional oxygen electrode for rechargeable Zn-Air batteries, Appl. Catal. B 294 (2021), 120239, https://doi.org/10.1016/j.apcatb.2021.120239.

[18] J.-C. Li, P.-X. Hou, S.-Y. Zhao, C. Liu, D.-M. Tang, M. Cheng, F. Zhang, H.-M. Cheng, A 3D bi-functional porous N-doped carbon microtube sponge electrocatalyst for oxygen reduction and oxygen evolution reactions, Energy Environ. Sci. 9 (2016) 3079–3084, https://doi.org/10.1039/C6EE02169G.

[19] L. Wei, H.E. Karahan, S. Zhai, H. Liu, X. Chen, Z. Zhou, Y. Lei, Z. Liu, Y. Chen, Amorphous Bimetallic Oxide–Graphene Hybrids as Bifunctional Oxygen Electrocatalysts for Rechargeable Zn–Air Batteries, Adv. Mater. 29 (2017) 1701410, https://doi.org/10.1002/adma.201701410.

[20] M. De Koninck, S.-C. Poirier, Bt Marsan, Cu$_x$Co$_{3-x}$O$_4$ Used as Bifunctional Electrocatalyst, J. Electrochem. Soc. 153 (2006) A2103, https://doi.org/10.1149/1.2338631.

[21] T. Zhao, S. Gadipelli, G. He, M.J. Ward, D. Do, P. Zhang, Z. Guo, Tunable Bifunctional Activity of Mn$_x$Co$_{3-x}$O$_4$ Nanocrystals Decorated on Carbon Nanotubes for Oxygen Electrocatalysis, ChemSusChem 11 (2018) 1295–1304, https://doi.org/10.1002/cssc.201800049.

[22] A. Azor, M.L. Ruiz-Gonzalez, F. Gonell, C. Laberty-Robert, M. Parras, C. Sanchez, D. Portehault, J.M. González-Calbet, Nickel-Doped Sodium Cobaltite 2D Nanomaterials: Synthesis and Electrocatalytic Properties, Chem. Mater. 30 (2018) 4986–4994, https://doi.org/10.1021/acs.chemmater.8b01146.

[23] H. Fu, M. Li, Q. Xu, G. Chen, Y. Zou, W. Zhang, S. Li, L. Ling, Nitrogen doped carbon-distributed and nitrogen-stabilized ultrafine FeM (M = Pd, Pt, Au) nanoclusters for doxorubicin detoxification, Appl. Catal. B 316 (2022), 121646, https://doi.org/10.1016/j.apcatb.2022.121646.

[24] K. Gong, F. Du, Z. Xia, M. Durstock, L. Dai, Nitrogen-doped carbon nanotube arrays with high electrocatalytic activity for oxygen reduction, Science 323 (2009) 760–764, https://doi.org/10.1126/science.1168049.

[25] T. Najam, S.S.A. Shah, W. Ding, J. Jiang, L. Jia, W. Yao, L. Li, Z. Wei, An Efficient Anti-poisoning Catalyst against SOx, NOx, and POx: P, N-Doped Carbon for Oxygen Reduction in Acidic Media, Angew, Chem., Int. Ed. 57 (2018) 15101–15106, https://doi.org/10.1002/ange.201808383.

[26] T. Najam, S. Ibraheem, M.A. Nazir, A. Shaheen, A. Waseem, M.S. Javed, S.S. A. Shah, X. Cai, Partially oxidized cobalt species in nitrogen-doped carbon nanotubes: Enhanced catalytic performance to water-splitting, Int. J. Hydr. Energy 46 (2021) 8864–8870, https://doi.org/10.1016/j.ijhydene.2021.01.016.

[27] T. Najam, S.S. Ahmad Shah, H. Ali, Z. Song, H. Sun, Z. Peng, X. Cai, A metal free electrocatalyst for high-performance zinc-air battery applications with good resistance towards poisoning species, Carbon 164 (2020) 12–18, https://doi.org/10.1016/j.carbon.2020.03.036.

[28] T. Najam, X. Cai, M.K. Aslam, M.K. Tufail, S.S.A. Shah, Nano-engineered directed growth of Mn3O4 quasi-nanocubes on N-doped polyhedrons: Efficient electrocatalyst for oxygen reduction reaction, Int. J. Hydrongen Engerg 45 (2020) 12903–12910, https://doi.org/10.1016/j.ijhydene.2020.02.205.

[29] Y. Liang, Y. Li, H. Wang, J. Zhou, J. Wang, T. Regier, H. Dai, Co3O4 nanocrystals on graphene as a synergistic catalyst for oxygen reduction reaction, Nat. Mater. 10 (2011) 780–786, https://doi.org/10.1038/nmat3087.

[30] J. Sun, H. Xue, Y. Zhang, X.-L. Zhang, N. Guo, T. Song, H. Dong, Y. Kong, J. Zhang, Q. Wang, Unraveling the Synergistic Effect of Heteroatomic Substitution and Vacancy Engineering in CoFe$_2$O$_4$ for Superior Electrocatalysis Performance, Nano Lett. 22 (2022) 3503–3511, https://doi.org/10.1021/acs.nanolett.1c04425.

[31] S.L. Zhang, B.Y. Guan, X.F. Lu, S. Xi, Y. Du, X.W. Lou, Metal Atom-Doped Co3O4 Hierarchical Nanoplates for Electrocatalytic Oxygen Evolution, Adv. Mater. 32 (2020) 2002235, https://doi.org/10.1002/adma.202002235.

[32] X. Liu, M. Park, M.G. Kim, S. Gupta, X. Wang, G. Wu, J. Cho, High-performance non-spinel cobalt–manganese mixed oxide-based bifunctional electrocatalysts for rechargeable zinc–air batteries, Nano Energy 20 (2016) 315–325, https://doi.org/10.1016/j.nanoen.2015.11.030.

[33] N. Sakai, K. Fukuda, R. Ma, T. Sasaki, Synthesis and Substitution Chemistry of Redox-Active Manganese/Cobalt Oxide Nanosheets, Chem. Mater. 30 (2018) 1517–1523, https://doi.org/10.1021/acs.chemmater.7b04068.

[34] G. Kresse, J. Hafner, Ab initio molecular dynamics for liquid metals, Phys. Rev. B 47 (1993) 558–561, https://doi.org/10.1103/PhysRevB.47.558.

[35] G. Kresse, J. Hafner, Ab initio molecular-dynamics simulation of the liquid-metal amorphous semiconductor transition in germanium, Phys. Rev. B 49 (1994) 14251–14269, https://doi.org/10.1103/PhysRevB.49.14251.

[36] J.P. Perdew, K. Burke, M. Ernzerhof, Generalized gradient approximation made simple, Phys. Rev. Lett. 77 (1996) 3865–3868, https://doi.org/10.1103/PhysRevLett.77.3865.

[37] G. Kresse, J. Furthmüller, Efficiency of ab-initio total energy calculations for metals and semiconductors using a plane-wave basis set, Comput. Mater. Sci. 6 (1996) 15–50, https://doi.org/10.1016/0927-0256(96)00008-0.

[38] P.E. Blöchl, Projector augmented-wave method, Phys. Rev. B 50 (1994) 17953–17979, https://doi.org/10.1103/PhysRevB.50.17953.

[39] G. Kresse, D. Joubert, From ultrasoft pseudopotentials to the projector augmented-wave method, Phys. Rev. B 59 (1999) 1758–1775, https://doi.org/10.1103/PhysRevB.59.1758.

[40] H.J. Monkhorst, J.D. Pack, Special points for Brillouin-zone integrations, Phys. Rev. B 13 (1976) 5188–5192, https://doi.org/10.1103/PhysRevB.13.5188.

[41] S.H. Talib, Z. Lu, X. Yu, K. Ahmad, B. Bashir, Z. Yang, J. Li, Theoretical Inspection of M1/PMA Single-Atom Electrocatalyst: Ultra-High Performance for Water Splitting (HER/OER) and Oxygen Reduction Reactions (OER), ACS Catal. 11 (2021) 8929–8941, https://doi.org/10.1021/acscatal.1c01294.

[42] Y. Tian, J. Julio Gutiérrez Moreno, Z. Lu, L. Li, M. Hu, D. Liu, Z. Jian, X. Cai, A synergetic promotion of sodium-ion storage in titania nanosheets by superlattice assembly with reduced graphene oxide and Fe-doping strategy, Chem. Eng. J. 407 (2021), 127198, https://doi.org/10.1016/j.cej.2020.127198.

[43] Y. Omomo, T. Sasaki, M. Wang, Watanabe, Redoxable Nanosheet Crystallites of MnO$_2$ Derived via Delamination of a Layered Manganese Oxide, J. Am. Chem. Soc. 125 (2003) 3568–3575, https://doi.org/10.1021/ja021364p.

[44] M. Osada, S. Yoguchi, M. Itose, B.-W. Li, Y. Ebina, K. Fukuda, Y. Kotani, K. Ono, S. Ueda, T. Sasaki, Controlled doping of semiconducting titania nanosheets for tailored spinelectronic materials, Nanoscale 6 (2014) 14227–14236, https://doi.org/10.1039/C4NR04465G.

[45] E. López-Fernández, J. Gil-Rostra, J.P. Espinós, A.R. González-Elipe, F. Yubero, A. de Lucas-Consuegra, Cu$_x$Co$_{3−x}$O$_4$ ultra-thin film as efficient anodic catalysts for anion exchange membrane water electrolysers, J. Power Sources 415 (2019) 136–144, https://doi.org/10.1016/j.jpowsour.2019.01.056.

[46] N. Heller-Ling, G. Poillerat, J.F. Koenig, J.L. Gautier, P. Chartier, Double channel electrode flow cell (DCEFC): application to the electrocatalysis of the oxygen reduction on oxide films, Electrochim. Acta 39 (1994) 1669–1674, https://doi.org/10.1016/0013-4686(94)85152-2.

[47] T. Najam, S. Shoaib Ahmad Shah, M. Sufyan Javed, P.-T. Chen, C. Chuang, A. Saad, Z. Song, W. Liu, X. Cai, Modulating the electronic structure of zinc single atom catalyst by P/N coordination and Co2P supports for efficient oxygen reduction in Zn-Air battery, Chem. Eng. J. 440 (2022), 135928, https://doi.org/10.1016/j.cej.2022.135928.

[48] Z. Wang, S. Xiao, Y. An, X. Long, X. Zheng, X. Lu, Y. Tong, S. Yang, Co(II)$_{1−x}$Co(0)$_{x/3}$Mn(III)$_{2x/3}$S Nanoparticles Supported on B/N-Codoped Mesoporous Nanocarbon as a Bifunctional Electrocatalyst of Oxygen Reduction/Evolution for High-Performance Zinc-Air Batteries, ACS Appl. Mater. Interfaces 8 (2016) 13348–13359, https://doi.org/10.1021/acsami.5b12803.

[49] S. Yang, Q. He, C. Wang, H. Jiang, C. Wu, Y. Zhang, T. Zhou, Y. Zhou, L. Song, Confined bimetallic phosphide within P, N co-doped carbon layers towards boosted bifunctional oxygen catalysis, J. Mater. Chem. A 6 (2018) 11281–11287, https://doi.org/10.1039/C8TA02897D.

[50] Q. Hu, B. Zhu, G. Li, X. Liu, H. Yang, C.D. Sewell, Q. Zhang, J. Liu, C. He, Z. Lin, Interconnected phosphorus-doped CoO-nanoparticles nanotube with three-dimensional accessible surface enables high-performance electrochemical oxidation, Nano Energy 66 (2019), 104194, https://doi.org/10.1016/j.nanoen.2019.104194.

[51] K. Yuan, D. Lützenkirchen-Hecht, L. Li, L. Shuai, Y. Li, R. Cao, M. Qiu, X. Zhuang, M.K.H. Leung, Y. Chen, U. Scherf, Boosting Oxygen Reduction of Single Iron Active Sites via Geometric and Electronic Engineering: Nitrogen and Phosphorus Dual Coordination, J. Am. Chem. Soc. 142 (2020) 2404–2412, https://doi.org/10.1021/jacs.9b11852.

[52] Y. Tong, P. Chen, T. Zhou, K. Xu, W. Chu, C. Wu, Y. Xie, A Bifunctional Hybrid Electrocatalyst for Oxygen Reduction and Evolution: Cobalt Oxide Nanoparticles Strongly Coupled to B,N-Decorated Graphene, Angew. Chem., Int. Ed. 56 (2017) 7121–7125, https://doi.org/10.1002/anie.201702430.

[53] X. Li, J. Wei, Q. Li, S. Zheng, Y. Xu, P. Du, C. Chen, J. Zhao, H. Xue, Q. Xu, H. Pang, Nitrogen-Doped Cobalt Oxide Nanostructures Derived from Cobalt–Alanine Complexes for High-Performance Oxygen Evolution Reactions, Adv. Funct. Mater. 28 (2018) 1800886, https://doi.org/10.1002/adfm.201800886.

[54] J. Masa, W. Xia, I. Sinev, A. Zhao, Z. Sun, S. Grützke, P. Weide, M. Muhler, W. Schuhmann, Mn$_x$Oy/NC and Co$_x$O$_y$/NC Nanoparticles Embedded in a Nitrogen-Doped Carbon Matrix for High-Performance Bifunctional Oxygen Electrodes, Angew. Chem. Int. Ed. 53 (2014) 8508–8512, https://doi.org/10.1002/anie.201402710.

[55] J.G. Chen, C.W. Jones, S. Linic, V.R. Stamenkovic, Best Practices in Pursuit of Topics in Heterogeneous Electrocatalysis, ACS Catal. 7 (2017) 6392–6393, https://doi.org/10.1021/acscatal.7b02839.

[56] A. Saad, D. Liu, Y. Wu, Z. Song, Y. Li, T. Najam, K. Zong, P. Tsiakaras, X. Cai, Ag nanoparticles modified crumpled borophene supported Co$_3$O$_4$ catalyst showing superior oxygen evolution reaction (OER) performance, Appl. Catal. B 298 (2021), 120529, https://doi.org/10.1016/j.apcatb.2021.120529.

[57] A. Saad, Y. Gao, A. Ramiere, T. Chu, G. Yasin, Y. Wu, S. Ibraheem, M. Wang, H. Guo, P. Tsiakaras, X. Cai, Understanding the Surface Reconstruction on Ternary WxCoBx for Water Oxidation and Zinc–Air Battery Applications, Small 18 (2022) 2201067, https://doi.org/10.1002/smll.202201067.

[58] A. Saad, Y. Gao, K.A. Owusu, W. Liu, Y. Wu, A. Ramiere, H. Guo, P. Tsiakaras, X. Cai, Ternary Mo$_2$NiB$_2$ as a Superior Bifunctional Electrocatalyst for Overall Water Splitting, Small 18 (2022) 2104303, https://doi.org/10.1002/smll.202104303.

[59] J. Deng, H. Li, J. Xiao, Y. Tu, D. Deng, H. Yang, H. Tian, J. Li, P. Ren, X. Bao, Triggering the electrocatalytic hydrogen evolution activity of the inert two-dimensional MoS2 surface via single-atom metal doping, Energy Environ. Sci. 8 (2015) 1594–1601, https://doi.org/10.1039/C5EE00751H.

[60] M.T.M. Koper, Thermodynamic theory of multi-electron transfer reactions: Implications for electrocatalysis, J. Electroanal. Chem. 660 (2011) 254–260, https://doi.org/10.1016/j.jelechem.2010.10.004.